Graphene plasmons in the presence of adatoms

2017 New J. Phys. 19 073027

(http://iopscience.iop.org/1367-2630/19/7/073027)

IOP Publishing New J. Phys. 19 (2017) 073027 https://doi.org/10.1088/1367-2630/aa7811

New Journal of Physics
The open access journal at the forefront of physics

Deutsche Physikalische Gesellschaft DPG
IOP Institute of Physics

Published in partnership with: Deutsche Physikalische Gesellschaft and the Institute of Physics

OPEN ACCESS

RECEIVED
13 February 2017

REVISED
15 May 2017

ACCEPTED FOR PUBLICATION
8 June 2017

PUBLISHED
25 July 2017

PAPER

Graphene plasmons in the presence of adatoms

Giovanni Viola[1], **Tobias Wenger**[1], **Jari Kinaret**[2] **and Mikael Fogelström**[1,3]

[1] Department of Microtechnology and Nanoscience (MC2), Chalmers University of Technology, SE-412 96 Göteborg, Sweden
[2] Department of Physics, Chalmers University of Technology, SE-412 96 Göteborg, Sweden
[3] Author to whom any correspondence should be addressed.

E-mail: mikael.fogelstrom@chalmers.se

Keywords: graphene plasmons, nonlocal response, graphene impurities, transport in graphene, plasmonic sensing

Abstract

We theoretically investigate graphene plasmons in the presence of a low density of adatoms on the graphene surface. The adatoms can significantly modify the conductivity and plasmonic properties of graphene and may produce a level splitting with the plasmon mode, resulting in two plasmon branches. The high energy branch exhibits large losses and the low energy branch exhibits low losses. Our model may also be considered as a simple model for molecules on graphene and we show that graphene plasmons are sensitive to such changes in the environment. Our microscopic treatment of plasmons and adatoms shows the sensitivity of plasmons and highlights the potential of graphene plasmons for sensing purposes.

1. Introduction

Graphene has recently emerged as an attractive plasmonic material at terahertz and mid-infrared frequencies [1–3]. Among the benefits of graphene as a plasmonic material are its tunable optical properties [4], low losses [5], and large confinement of electromagnetic fields under the right conditions. Field localization by a factor of up to 200 has been predicted [6] which facilitates strong light–matter interactions [7]. Considering that large field localization leads to large plasmon losses, a more conservative estimate of the field localization is $1/\alpha$, where $\alpha \approx 1/137$ is the fine-structure constant [6, 8].

Recently, graphene plasmons have been studied using nanotips [9, 10], subwavelength gratings [11–13], metal nanoantennas [14, 15] and nanoribbons [16]. Possible applications include label-free molecular sensing [17, 18], photonic modulators [14, 19], as well as ultrafast photodetectors [20], showcasing the versatility of graphene as a plasmonic material.

However, the quality of graphene still limits many proposed applications [21], and high quality graphene devices are labor-intensive to fabricate. Even the cleanest graphene samples exhibit some momentum relaxation [22], and thus a theoretical analysis of various loss mechanisms is of much interest [23–28]. The high frequency relaxation is of fundamental importance since the plasmons of interest are in this regime. Graphene conductivity in a relaxation time approximation [29, 30] was investigated by Rana [31] and by Jablan *et al* [5] who found substantial plasmon losses for realistic relaxation times. This was also found in the experiments by Chen *et al* [9] and by Fei *et al* [10].

Graphene has previously been considered for sensing purposes, see for instance [32, 33], and the large surface-to-volume ratio is one of the main advantages of graphene in this regard. Chemical sensing has been explored in the mid-infrared part of the spectrum where plasmons have been exploited to detect changes in refractive indices [34, 35] and vibrational states in biomolecules [18, 36]. These applications show much promise for plasmonic-based sensing in the future. However, also electronic transitions in atoms and molecules can couple to graphene plasmons but have so far not been analyzed in detail. Electronic properties of molecules and atoms that adsorb on the graphene surface have been studied extensively using various computational methods [37–42] and different substances have different coupling strengths and energy of the electronic levels. This variability between substances makes it possible to consider graphene plasmonic-based sensors which have the ability to selectively detect various compounds. We use these previous results to investigate adatom effects on the

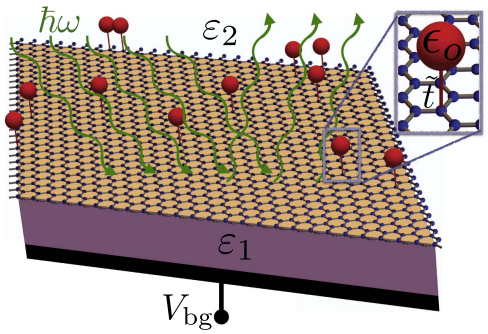

Figure 1. Schematic view of the studied system. An infinite sheet of graphene is decorated by a dilute random distribution of adatoms, coupled to graphene by tunneling. The adatoms, here represented by the red spheres, are described by three phenomenological parameters: the energy level, ϵ_0, measured with respect to the Dirac point, an intrinsic lifetime δ^{-1}, and a matrix element $\tilde{t}$ describing the electron hopping between graphene and an individual adatom. The dielectric material on the two sides of the graphene have the relative permittivities ε_1 and ε_2, respectively. The back gate $V_{\rm bg}$ makes it possible to tune the Fermi energy in the graphene. Inset: zoom on the adatom with the hopping element represented with a red vertical bond.

plasmonic properties of graphene. Our approach is complementary to previous works on plasmonic-based sensing in graphene as we study the plasmon response to microscopic degrees of freedom, rather than to changes in the dielectric environment [35] or to vibrational modes [18, 36, 43].

In this article we develop and analyze a model for uncorrelated adatoms, coupled to the graphene surface by tunneling (see figure 1). Since the adatoms are not the only imperfections in graphene we also include an electron relaxation time which we include in a number conserving manner following the Mermin prescription [5, 29]. This relaxation time describes, phenomenologically, all sources of damping except the adatoms we are investigating. We explore the effects of adatoms on the single-particle properties of graphene as well as on the conductivity. We focus on the graphene surface plasmon mode and investigate its dispersion and the related losses. We find that plasmons close to resonance with the transition from the adatom energy level to above the Fermi energy become lossy. Furthermore, depending on the density of adatoms, their presence can split the plasmon mode into two separate branches, one low energy branch which experiences low losses and one high energy branch experiencing high degree of losses. We discuss how this can be used for ultra-sensitive sensing under the right conditions.

The article is organized as follows: in section 2 we treat the graphene plasmon dispersion and the graphene loss function. In section 3 we develop a manybody description of the system and derive an expression for the nonlocal longitudinal conductivity $\sigma(q,\,\omega)$. Finally, in section 4 we analyze the effects of the adatoms on plasmons, in particular on the plasmon dispersion relation and damping. In appendix A we present a derivation of two central equations in the article, equations (3) and (4). Appendix B gives details of the microscopic model and in appendix C a simplified expression for the susceptibility tensor is derived, from which the conductivity is obtained. Throughout the article we use $\hbar = c = 1$.

2. Graphene plasmons

Longitudinal plasmons confined at a conducting interface between two dielectrics with relative dielectric constants ε_1 and ε_2 satisfy the dispersion relation [5, 6]

$$\frac{\varepsilon_1}{\kappa_1(q,\,\omega)} + \frac{\varepsilon_2}{\kappa_2(q,\,\omega)} + \frac{\mathrm{i}\sigma(q,\,\omega)}{\omega\varepsilon_0} = 0, \tag{1}$$

where $\kappa_{1,2}(q,\,\omega) = \sqrt{q^2 - \varepsilon_{1,2}\,\omega^2/c^2}$ and ε_0 is the vacuum dielectric constant. Here $\sigma(q,\,\omega)$ is the longitudinal nonlocal conductivity of the graphene layer. The longitudinal conductivity describes the response to a longitudinal electric field meaning that $\mathbf{q}$ and $\boldsymbol{E}$ are parallel and $|\mathbf{q}| = q$. In the non-retarded limit, $q \gg \sqrt{\varepsilon_{1,2}}\,\omega/c$, equation (1) reduces to the simpler expression

$$\frac{(\varepsilon_1 + \varepsilon_2)}{q} + \frac{\mathrm{i}\sigma(q,\,\omega)}{\varepsilon_0\omega} = 0. \tag{2}$$

This is a good approximation as long as the wavelength of the mode is much smaller than the free space wavelength, which is the regime we are investigating.

In general equation (2) is a complex equation and for any given ω it can be solved by allowing complex wave vectors, $q = q_1 + \mathrm{i}q_2$. Physically this means that the corresponding oscillation of the mode is damped. For weak damping, we can expand equation (2) in small q_2/q_1, and separating the real and imaginary parts of the

conductivity, $\sigma(q,\,\omega) = \sigma_1(q,\,\omega) + \mathrm{i}\sigma_2(q,\,\omega)$, we obtain to lowest order in q_2

$$\varepsilon_1 + \varepsilon_2 - \frac{q_1\sigma_2(q_1,\,\omega)}{\omega\varepsilon_0} = 0, \tag{3}$$

$$\frac{q_2}{q_1} = \frac{\sigma_1(q_1,\,\omega)}{\frac{\partial}{\partial_{q_1}}(q_1\sigma_2(q_1,\,\omega))} = \frac{\sigma_1(q_1,\,\omega)}{\varepsilon_0(\varepsilon_1+\varepsilon_2)\omega/q_1 + q_1\partial_{q_1}\sigma_2(q_1,\,\omega)}, \tag{4}$$

under the assumption that no losses are present in the substrate, i.e. $\varepsilon_{1,2}$ are real. For a more detailed derivation of equations (3) and (4), see appendix A. Equation (3) is identical to equation (2) with the assumption of no losses, i.e. $\sigma_1(q_1,\,\omega) = 0$. The plasmon losses are given by equation (4) and in the second equality we have used equation (2) to express $\sigma_2(q,\,\omega)$ on the plasmon mode. Equations (3) and (4) show explicitly that in the low-loss limit the graphene plasmon dispersion is determined by $\sigma_2(q,\,\omega)$ while the plasmon losses are given by the ratio $\sigma_1(q,\,\omega)$ to the effective velocity $v_{\mathrm{eff}} = \frac{\omega}{q_1} + \frac{q_1\partial_{q_1}\sigma_2(q_1,\omega)}{\varepsilon_0(\varepsilon_1+\varepsilon_2)}$ times $\varepsilon_0(\varepsilon_1+\varepsilon_2)$. The effective velocity is given by the plasmon phase velocity ω/q_1 and a nonlocal correction given by the q_1 derivative of $\sigma_2(q_1,\,\omega)$. The smaller the effective velocity, the higher the dissipative loss.

An alternative way to describe plasmons is to analyze the imaginary part of the current–current correlation function evaluated in the random-phase approximation. This is the spectral function of current fluctuations and describes where in $q-\omega$ space it is possible to deposit energy. For this reason it is sometimes called the loss function and it is defined as [30, 44]

$$S_{j_x}(q,\,\omega) \equiv -\frac{1}{v_j}\,\mathrm{Im}\left[\frac{1}{\varepsilon(q,\,\omega)}\right] = \frac{\omega\sigma_1(q,\,\omega)}{\left|1+\frac{\mathrm{i}qe^2\sigma(q,\omega)}{\omega\varepsilon_0(\varepsilon_1+\varepsilon_2)}\right|^2} \tag{5}$$

with $v_j = \frac{e^2q}{\varepsilon_0(\varepsilon_1+\varepsilon_2)\omega^2}$. The loss function has peaks where equation (2) is satisfied and these peaks are interpreted as signatures of the plasmons [30].

The plasmon dispersion, i.e., solutions to equations (3) and (4) as well as the loss function are discussed in section 4. First, the conductivity of graphene with adatoms needs to be calculated.

3. Microscopic model for graphene conductivity

The system considered consists of a pristine infinite graphene sheet [45, 46] where momentum relaxation is added to model losses in graphene [5, 29]. We introduce the convention that clean graphene means graphene with the finite momentum relaxation. To the clean graphene, we add a dilute distribution of identical adatoms that are modeled as non-magnetic Fano-Anderson localized states [30] coupled to graphene by tunneling as sketched in figure 1. When the coverage is dilute, correlations between adatoms are unimportant, and each adatom can be considered independently. Here, dilute means $n_{\mathrm{imp}} \ll 1$, where n_{imp} is the fraction of adatoms per lattice site. The total system can be described by a tight binding Hamiltonian that includes the tight binding Hamiltonian of graphene, the Hamiltonian of the adatoms, and the hopping between graphene and adatoms. Effective hopping Hamiltonians for different adatoms on graphene are obtained in [39–42], by use of DFT modeling of the composed system. In the following we assume a spin degenerate system, where the spin degree of freedom is included as a spin degeneracy factor $g_s = 2$. An individual adatom is situated on the graphene atom at site $\mathbf{x}$ connected to a single graphene lattice site by a hopping parameter $\tilde{t}$. The adatom has a single energy level at ϵ_0, measured relative to the charge neutrality point of clean graphene, and has an intrinsic lifetime δ^{-1}. These are phenomenological parameters that are inputs of the model and in this section we explore the general features of the model for various adatom parameters. In section 4 we obtain parameters for hydrogen from [40] to examine a simple adatom.

The Hamiltonian of the system with a single adatom is

$$\hat{H} = \epsilon_0\hat{d}^\dagger\hat{d} + \sum_{\langle\mathbf{i},\mathbf{i}'\rangle} t_0\hat{\psi}_{\mathbf{i}'}^\dagger\hat{\psi}_{\mathbf{i}} + \tilde{t}\;\hat{d}^\dagger\hat{\psi}_x + \mathrm{h.c.}, \tag{6}$$

where $\hat{d}$ is the annihilation operator for the electron on the adatom and $\hat{\psi}_{\mathbf{i}}$ is the annihilation operator of graphene electrons on site $\mathbf{i}$. The sum in equation (6) is over all nearest neighbor sites of the graphene lattice and t_0 is the corresponding hopping parameter. The Hamiltonian is quadratic in the operators and can be diagonalized also for the case of a dilute density of adatoms, see appendix B for details.

In the regime of dilute density of adatoms and in the Dirac approximation, the Green's function of the Hamiltonian is given by [47]

$$G_0^R(\mathbf{p},\,\epsilon) = \sum_{\lambda=\pm}\frac{g_{0,\lambda}^R(\mathbf{p},\,\epsilon)}{2}\begin{pmatrix}1 & \lambda\mathrm{e}^{-\mathrm{i}\phi_p}\\ \lambda\mathrm{e}^{\mathrm{i}\phi_p} & 1\end{pmatrix}, \tag{7a}$$

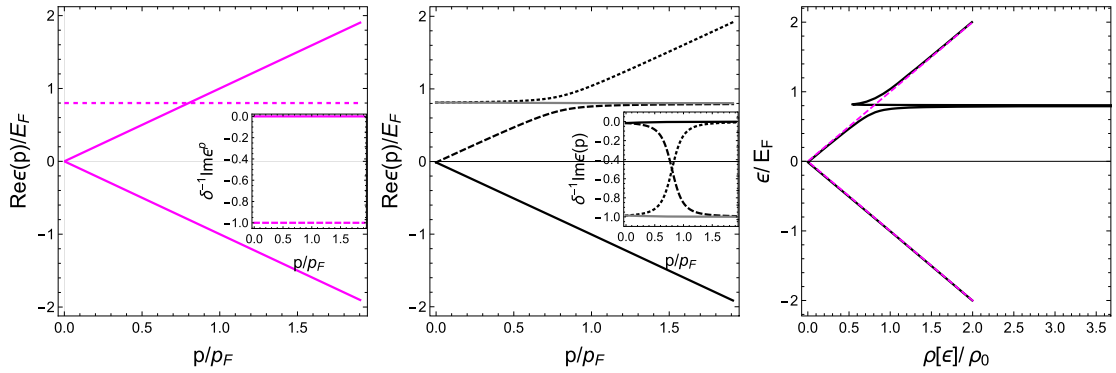

Figure 2. Left: linear energy bands of pristine graphene (solid magenta) and the momentum independent adatom energy level (dashed magenta). Center: the real part of the Green's function poles $\epsilon_\lambda^\pm(\mathbf{p})$ as function of momentum, inset the imaginary part. The adatoms introduce a splitting of the positive energy graphene band. The splitting introduces a hybridization of the bare graphene and bare adatom energy levels, resulting in the level repulsion between the states. Right: density of states for clean graphene in dashed magenta and black solid line in the presence of the adatoms with $\rho_0 = \rho(E_F)$. The peak in the density of states reflects the presence of the flat adatom energy level. The parameters in all panels are $\epsilon_0 = 0.8E_F$, $\delta = 0.001E_F$ and $t = 0.1E_F$.

$$g^R_{0,\lambda}(\mathbf{p},\,\epsilon) = \frac{1}{\epsilon^+ - \lambda E_\mathbf{p} - \Sigma^R_{\rm imp}(\epsilon)}, \qquad \phi_p = \arctan\frac{p_x}{p_y}, \tag{7b}$$

$$\Sigma^R_{\rm imp}(\epsilon) = \frac{|t|^2}{(\epsilon^+ - \epsilon_0 + {\rm i}\delta)}, \qquad \epsilon^+ = \epsilon + {\rm i}0^+, \tag{7c}$$

where $|t|^2 = n_{\rm imp}\,|\tilde{t}|^2$ and $n_{\rm imp}$ is the fraction of adatoms per lattice site. The effect of the adatoms is captured by the self-energy $\Sigma^R_{\rm imp}(\epsilon)$. The poles of the single-particle Green's function define the single-particle states and in the presence of the adatoms the resulting single-particle bands are hybridized between the bare adatoms and bare graphene single-particle energy bands $\lambda E_\mathbf{p}$, where $\lambda = \pm$ is the graphene band index. The poles of the retarded Green's function and the renormalization factors are found to be

$$\epsilon^\pm_\lambda(\mathbf{p}) = \frac{\lambda E_\mathbf{p} + \epsilon_0 - {\rm i}\delta \pm \sqrt{(\lambda E_\mathbf{p} - \epsilon_0 + {\rm i}\delta)^2 + 4|t|^2}}{2},$$
$$Z^\pm_\lambda(\mathbf{p}) = \frac{1}{2} \pm \lambda\frac{E_\mathbf{p} - \epsilon_0 + {\rm i}\delta}{2\sqrt{(\lambda E_\mathbf{p} - \epsilon_0 + {\rm i}\delta)^2 + 4|t|^2}},$$

where the renormalization factors $Z^\pm_\lambda(\mathbf{p})$ are the residues of the poles, i.e. $Z^\pm_\lambda(\mathbf{p}) = {\rm Res}[G^R_0(\mathbf{p},\,\epsilon)]|_{\epsilon^\pm_\lambda(\mathbf{p})}$. The energies $\epsilon^\pm_\lambda(\mathbf{p})$ are shown in the center panel of figure 2. Due to the hybridization between the graphene bands and adatoms there is a level repulsion around ϵ_0, close to which the hybridization is strong and gives rise to a finite lifetime of the order δ^{-1} to the energy bands. Far from the level splitting, the energy states approach their uncoupled behaviors. The right panel of figure 2 shows the total density of states of the coupled system which exhibits a significant deviation close to the level splitting compared to the pristine graphene case. Specifically, there is a significant increase in the density of states close to ϵ_0 due to the coupling to the adatoms. The change of the bands compared to pristine graphene opens up new possible electronic transitions that alter the conductive and plasmonic properties of graphene, as discussed in the following.

The conductivity of the system can be computed using the Green's function in equation (7*a*). This is achieved by calculating the current response to an electric field $\boldsymbol{E}(\mathbf{x},\,t) = \boldsymbol{E}_\mathbf{q}{\rm e}^{{\rm i}(\mathbf{q}\cdot\mathbf{x}-\omega t)}$ (t is time in this paragraph, not to be confused with the coupling above). We restrict our analysis to the response to a longitudinal electric field which in the temporal gauge, $\phi(\mathbf{x},\,t) = 0$, is given by $\boldsymbol{E}(\mathbf{x},\,t) = -{\rm i}\omega\boldsymbol{A}(\mathbf{x},\,t)$. We set the electric field, $\boldsymbol{E}$, and the momentum, $\mathbf{q}$, to be parallel to the x-axis. According to minimal substitution [30], the perturbation given by the field $\boldsymbol{E}$ is $\delta\hat{H}_x = ev_F A_q\hat{j}_x(\mathbf{q}){\rm e}^{{\rm i}(qx-\omega t)}$ where $\hat{j}_x(\mathbf{q}) = ev_F\sum_\mathbf{p}\hat{\psi}^\dagger_{\mathbf{p}-\mathbf{q}}\sigma_x\hat{\psi}_\mathbf{p}$ is the longitudinal current operator [45, 46, 48]. The diamagnetic current is zero in the Dirac approximation [48]. The conductivity of the system can be obtained from the current–current response function (longitudinal susceptibility) which relates the average value of the current to the vector potential to linear order $\langle\hat{j}_x(\mathbf{q},\,\omega)\rangle = \chi_{j_xj_x}(\mathbf{q},\,\omega)A_q$ [30, 49]. From this expression and the relationship between the vector potential and the electric field, the conductivity can be seen to be $\sigma(\mathbf{q},\,\omega) = \frac{\rm i}{\omega}\chi_{j_xj_x}(\mathbf{q},\,\omega)$. The current–current response can be expressed in terms of the Green's function as

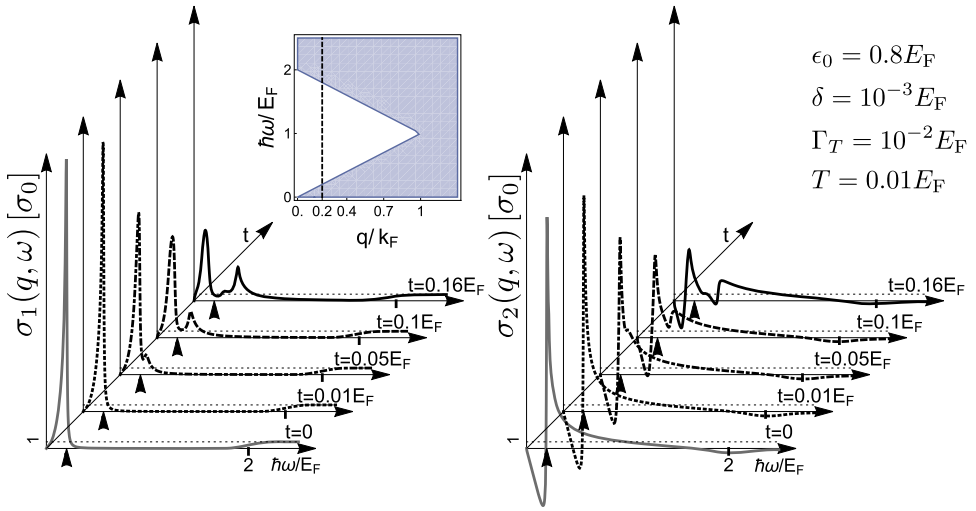

Figure 3. The nonlocal conductivity $\sigma(q,\omega)$ as a function of frequency ω with $q = |E_F - \epsilon_0|/v_F$ for different values of the hopping parameter t. The plots are for a constant wave vector $q = 0.2k_F$, shown by the dashed line in the inset, where the white triangle shows the Pauli blocked region for zero temperature. Real part of the conductivity is shown in the left panel and the imaginary part is shown in the right panel. Note that the scale on the t axes is not linear. The deviation of the conductivity from the clean case is hardly visible for $t < k_B T$, but for larger values of t there are structures appearing that significantly modify the conductivity. The conductivity is shown in units of $\sigma_0 = e^2/(4\hbar)$.

$$\chi_{j_x j_x}(\mathbf{q},\omega) = g_s g_v \frac{ie^2 v_F^2}{2}\int \frac{d\mathbf{p}d\epsilon}{(2\pi)} \mathrm{Tr}[\sigma_x G_0^R(\mathbf{p},\epsilon)\sigma_x G_0^K(\mathbf{p}-\mathbf{q},\epsilon-\omega) + \sigma_x G_0^K(\mathbf{p},\epsilon)\sigma_x G_0^A(\mathbf{p}-\mathbf{q},\epsilon-\omega)], \quad (8)$$

where $g_s g_v$ is the total spin-valley degeneracy factors, see appendix C for details. In pristine graphene, $\Sigma^R_{\mathrm{imp}}(\epsilon) = -i0^+$, the energy integral in equation (8) can be performed analytically to arrive at the expression considered in [50–53]. In the temporal gauge the zero frequency component of the response is unphysical and has to be removed to avoid having a response to a static vector potential [53]. In the following we present results for electron doped graphene and when adatoms are present we take ϵ_0 to be positive (with respect to the Dirac point). However, our model can also be applied for hole doped graphene and/or negative ϵ_0.

Before analyzing the conductivity in the presence of the adatoms it is useful to examine the conductivity for pristine graphene. In the pristine case there exists a Pauli blocked triangle, inside which plasmon losses vanish at zero temperature due to the real part of the conductivity being identically zero [3, 6, 50, 51]. This triangle in (q,ω)-space is shown in the inset of figures 3 and 4. For non-zero temperatures or when momentum relaxation is included, e.g. through a finite relaxation time, the triangle is no longer completely lossless but for moderate temperatures and relaxation times it is still the region where plasmons with low losses are expected to exist [5]. In this article we take the momentum relaxation time (Γ^{-1}) to be 1 ps, as reported in [54]. This relaxation time accounts for all intrinsic relaxation channels of the graphene and we include this in a number conserving way following the Mermin prescription [5, 29]. As already introduced, we refer to graphene with the finite relaxation time as clean graphene to distinguish from graphene together with the adatoms (and also a relaxation time).

The calculated conductivity in the presence of adatoms is shown in figure 3 for various values of the hopping parameter t and an impurity energy fixed at $\epsilon_0 = 0.8E_F$, i.e., the energy level of the adatoms is close the Fermi energy. The presence of adatoms with energies close to the Fermi energy has an effect on the conductivity for frequencies close to the transition frequency $|E_F - \epsilon_0|$ between the adatom energy level and the Fermi energy. In particular there are peaks that appear inside the originally lossless triangle, which will give rise to larger plasmons losses, see equation (4). The imaginary part of the conductivity is also changed which will lead to changes in the plasmon dispersion as can be seen from equation (3).

Figure 4 shows the conductivity for an increasing adatom energy level detuning from the Fermi energy and a fixed density of adatoms. As the energy level moves further from the Fermi energy the conductivity becomes more and more like the conductivity of clean graphene and the effect of the adatoms becomes negligible. From this we conclude that for the adatoms to have a large effect, the energy level of the adatoms needs to be close to the Fermi energy.

The new features that are present in the conductivity, as shown in figures 3 and 4, arise from the modification of the graphene bands caused by the presence of adatoms which is visible in figure 2. This modification of the conduction band around ϵ_0 changes the possible electronic transitions and in particular the allowed intraband transitions within the conduction band. These new transitions start playing a role around energies

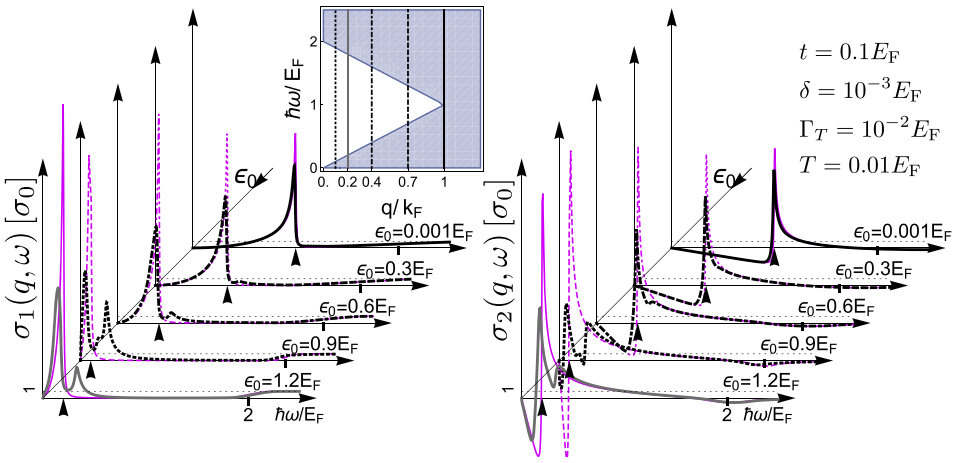

Figure 4. The effects of the detuning $|E_F - \epsilon_0|$ on the conductivity. The figure at the left shows $\sigma_1(q, \omega)$ versus ω while the figure at the right shows $\sigma_2(q, \omega)$ versus ω. Different lines correspond to different values of the adatom energy level (ϵ_0) and $q = |E_F - \epsilon_0|/v_F$. The corresponding cuts in the $q - \omega$ plane are shown in the inset, and the upward arrows indicate the point where ω enters the Pauli blocked triangle. The effect of the adatoms is reduced with increased distance between E_F and ϵ_0. The thin magenta lines correspond to $\sigma_1(q, \omega)$ for clean graphene. The conductivity is shown in units of $\sigma_0 = e^2/(4\hbar)$.

$\omega \approx |E_F - \epsilon_0|$, which is where there is enough energy for electrons to transition from the modified part of the band to unoccupied parts of the band above E_F. This is the frequency around which the changes in conductivity start occurring.

4. Graphene plasmons in the presence of a dilute density of adatoms

For concreteness, in this section we set the adatom parameters to be $\tilde{t} = 7.5$ eV, $\epsilon_0 = 0.16$ eV, and $\delta = 10^{-3}E_F$, see appendix B for more details. These parameters are extracted from [40] for hydrogen adsorbed on graphene. The individual hopping parameter, $\tilde{t}$, is large compared to the other energies but in the dilute adatom case the relevant parameter $t^2 = n_{\text{imp}}\tilde{t}^2$ is small for the densities we consider. Hydrogen is chosen since it is a simple atom and can serve as a typical atom adsorbed on the graphene. We emphasize that our model can be applied for other types of atoms and even simple molecules as well.

As stated previously, the loss function exhibits peaks where the dispersion equation has solutions. Figure 5 shows the loss function for an adatom density on the graphene of $n_{\text{imp}} = 10^{-5}$ per graphene lattice site (approximately 300 adatoms per μm^2). The magenta line shown in figure 5 is the plasmon dispersion obtained by solving equation (3) for clean graphene. The peak of the loss function and the solution to the dispersion equation are in good agreement. The exception is close to the gray dashed line where the deviation is significant and a level splitting occurs. The level splitting between the bare plasmon and the bare adatom is caused by the coupling of adatoms to the graphene surface. The energy around which the level splitting occurs is represented in the figure as the horizontal dashed gray line. This energy represents the energy needed to excite an electron from the adatom energy to above the Fermi energy.

To examine the effect of adatoms on the plasmons in more detail, the left panel of figure 6 shows a zoom of the loss function from figure 5 which is centered on the splitting. The red dashed line in the figure is the solution to the dispersion equation, equation (3), for the same density of adatoms as the loss function and the solid red line is the obtained loss, q_2, from equation (4). The level splitting is accompanied by large plasmons losses and an emergence of two separate plasmon branches. The low energy plasmon branch exhibits low losses and the high energy branch has a large amount of accompanying loss. The larger loss in the upper branch can be understood by considering the Fermi golden rule, a new loss channel is opened for the plasmons in this branch. The loss channel is the excitation of a single electron around the adatom energy (of which there are many, see the DoS in figure 2) to above the Fermi energy where there are unoccupied electron states. The plasmons in the low energy branch do not have enough energy to lose energy through this channel. On resonance with this transition there is a very pronounced plasmons loss which separates the plasmon branches.

The right panel of figure 6 shows the evolution of a loss function cut at $q/k_F = 0.013$ as the density of adatoms is varied. This particular cut is chosen to show the loss function evolution for this particular adatom species (hydrogen) as clearly as possible. For small values of adatom density, there is only one plasmon peak visible, but as the density increases, the splitting into two branches is visible in the two emergent peaks. The separation between the two peaks grows as the adatom density is increased even further.

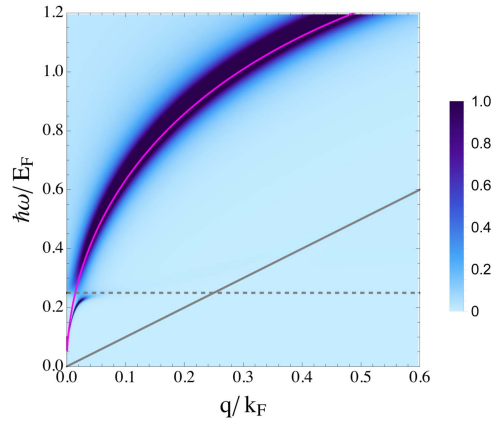

Figure 5. The loss function $S_{j_x}(q, \omega)$ with a density of adatoms together with the dispersion relation for clean graphene, shown by the magenta line. The peak of the loss functon is in good agreement with the clean dispersion except in the low energy, low q corner. The results in this figure are calculated for $E_F = 0.2$ eV, $T = 30$ K, adatom density 300 μm^{-2}, and $\varepsilon_1 = \varepsilon_2 = 1$. The solid gray line shows the edge of the Pauli blocked triangle and the dashed gray line shows the value of $\omega \simeq |E_F - \epsilon_0| + t/2$ around which there is a level splitting.

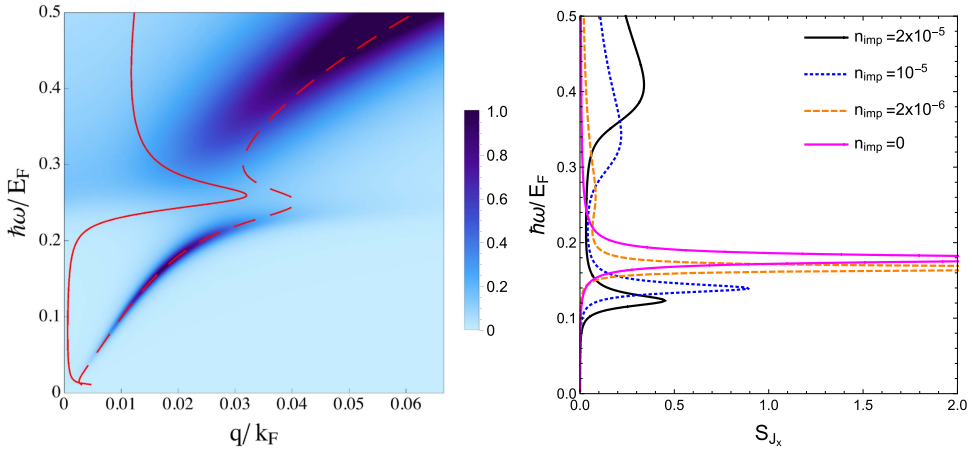

Figure 6. Left: small $q - \omega$ corner zoom of figure 5 that highlights the level splitting of the plasmon mode. The red dashed line shows the plasmon dispersion obtained by solving equation (3) and the red solid line shows the losses obtained from equation (4). The color scale shows the value of the loss function for the same parameters as the dispersion in order to enhance the splitting effect. Right: vertical cuts of the loss function for different adatom densities to show the evolution of the splitting. The cut is taken for $q/k_F = 0.013$ for maximal visibility of the splitting in the different curves. The blue dotted line is a cut from the loss function in the left figure. The other curves show how the splitting vanishes for small adatom densities and the emergence of the two branches for large densities.

To explore the adatom effect on plasmons in a large frequency range, figure 7 shows the plasmon propagation length along the dispersion until it crosses into the single-particle continuum. The plasmon propagation length (defined as the distance covered until the intensity of the plasmon falls by e^{-1} [6]) in units of the plasmon wavelength, L_p/λ_p, can be obtained from the ratio q_1/q_2 in equation (4) as $L_p/\lambda_p = q_1/(4\pi q_2)$. Note that the plasmon wavelength is $\lambda_p = 2\pi/q_1$.

Both panels of figure 7 show the plasmon propagation length as a function of frequency for different adatom densities on the graphene. The left panel is calculated for $E_F = 0.2$ eV ($k_F \simeq 1/(3.3\,\text{nm})$) and the right panel is calculated for $E_F = 0.4$ eV ($k_F \simeq 1/(1.65\,\text{nm})$). The propagation lengths for clean graphene in both cases are shown in figure 7 as the magenta lines. The reason for the different propagation lengths in the two panels is that the relevant parameter for damping in the clean case is Γ/E_F. The plasmons are significantly affected by the presence of adatoms, in particular the damping is increased for energies above the transition frequency to excite electrons from the adatom energy level to above the Fermi energy. In the left panel of figure 7, this energy is roughly $0.2E_F$, which corresponds to $\epsilon_0 = 0.16$ eV (hydrogen), and $E_F = 0.2$ eV. By changing the Fermi energy, the energy needed to make a transition to an unoccupied state changes. Therefore the energy at which the propagation length shows a step is different in the left and right panels of figure 7. For large enough densities, this step is where the plasmon is split into two branches.

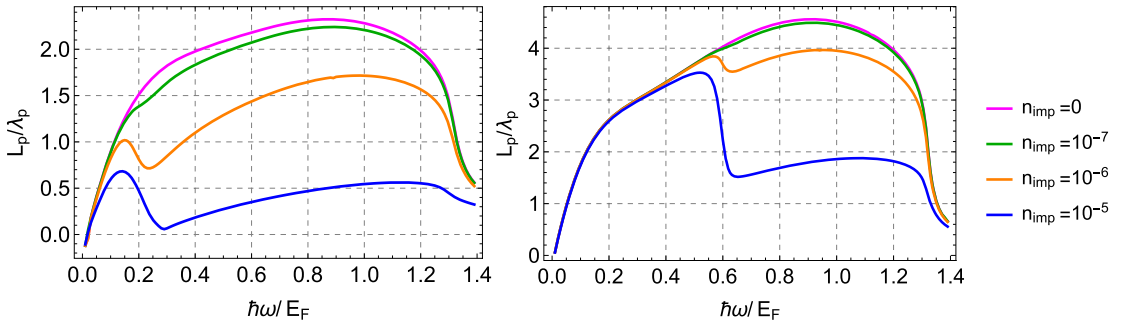

Figure 7. Plasmon propagation length, L_p/λ_p, computed using equations (3) and (4), versus $\hbar\omega$ for different adatom densities. The left panel is calculated for $E_F = 0.2$ eV and the right panel for $E_F = 0.4$ eV. The magenta lines represent clean graphene, green line $n_{\rm imp} = 10^{-7}$, orange line $n_{\rm imp} = 10^{-6}$, and blue line $n_{\rm imp} = 10^{-5}$. This corresponds to approximately 3 μm^{-2}, 30 μm^{-2}, and 300 μm^{-2} respectively. The sharp drop around $1.3E_F$ is due to the plasmon dispersion crossing into the particle-hole continuum where the plasmon becomes heavily damped.

The left and right panel of figure 7 are obtained for identical parameters except for the Fermi energy. The left panel clearly shows a larger effect for the same density of adatoms compared to the right panel. The conclusion is that for sensing purposes the Fermi energy should be tuned close to the adatom energy level for the sensitivity to be large.

5. Discussion

In this article we have focused on the graphene plasmon properties and how they are influenced by small densities of adatoms on the graphene surface. The induced plasmon losses and the level splitting that we find can be probed by for example light scattering in a grating environment [11], or on patterned graphene microribbons [1]. For a properly dimensioned grating or microribbon array, it would be possible to perform a laser frequency sweep and measure optical signatures of the presence of the adatoms as seen in figure 6. For the doping levels considered in this article, the typical dimension of the grating periodicity or the microribbon arrays needed are on the order of a few hundred nanometers. An alternative route to investigate the plasmons is by nanotip experiments such as in [9, 10], where the number of plasmon oscillations are measured. Obtaining such data for different frequencies could reveal the presence of small amounts of adatoms and their energy levels.

Our analysis is restricted to the presence of a single kind of adatom, i.e., all the adatoms on the surface are characterized by the same ϵ_0, $\tilde{t}$, and δ. In our model, the values of ϵ_0, $\tilde{t}$, and the adatom density determine the characteristic level splitting that separates the two plasmon branches, see figures 6 and 7. Also, the sensitivity of the plasmons to the adatoms is found to be large when the adatom energy is close to the Fermi energy. Hence, by measuring the plasmonic properties and taking advantage of the tunability of E_F offered by graphene, it is possible to determine ϵ_0 and thus discriminate between different adatoms. We stress that different adatoms exhibit different values of ϵ_0 as indicated by DFT calculations, see [37–42, 55], and that our model is general enough to handle various adatoms and simple molecules. Our model thus enables selective sensing of various adatoms and molecules by probing the plasmonic properties of graphene. It should be noted that the adatom densities involved, 30–300 μm^{-2}, is enough to increase plasmon losses and create a level splitting, making sensing of minute amounts of substances possible using graphene plasmons coupled to electron energy levels of adatoms. This is an increase of 2–3 orders of magnitude in sensitivity compared to experimental results for biomolecules obtained in [36], where plasmon coupling to vibrational modes of molecules was utilized for sensing. In our model, the adatom densities needed to produce a measurable plasmon response depends on the adatom coupling strength, $\tilde{t}$, which is considered as an input in our model. Thus, the sensitivity of the proposed sensing scheme is different for different adatoms. Adatoms that couple strongly to graphene will give rise to larger plasmon response for a given density than weakly coupled adatoms.

In this article we have taken a view towards sensing of the adatoms on the graphene surface. However, the adatoms may also be considered as imperfections on the graphene that impedes electron propagation by allowing the electrons to tunnel onto the adatom. For the purpose of plasmonics, long propagation lengths are often sought after and such damping is unwanted. We find that even small amounts of adatoms may have a significant effect on the plasmon damping. This is potentially one of several mechanisms that induces the large plasmon damping found in experiments [9, 10].

6. Conclusions

We have investigated how graphene plasmons are affected by adatoms by comparing plasmons in realistic quality graphene with and without adatoms. We found that adatoms with energy levels close to the Fermi energy induces a strong level splitting between the bare plasmon mode and the adatom energy level. This level splitting is accompanied by large plasmon losses and depending on the adatom density may separate the plasmon mode into two separate branches, one low energy branch and one high energy branch. The low energy branch is virtually unaffected by the presence of the adatoms, whereas the high energy branch experiences larger losses. This is due to a new plasmon decay channel opening up, namely the excitation of an adatom electron to an unoccupied state above the Fermi energy.

Furthermore, we studied the sensitivity of the plasmon losses to the presence of adatoms. As a typical atom, we considered hydrogen and we found that a density of 300 adatoms per μm^2 is enough to give rise to a significant level splitting, and already 30 adatoms per μm^2 is enough to damp the upper branch. These effects could be measured in various light scattering experiments using dielectric gratings as well as using nanotips, making it possible to envision ultra-sensitive devices that measure the plasmon dispersion and losses to infer the presence of adatoms and molecules on the graphene surface.

Our results highlight the sensitivity of graphene plasmons to microscopic degrees of freedom and the possibility to use this effect in applications. Microscopic models for coupling various degrees of freedom to the plasmons is a very rich field and has the potential to further increase the already large sensing potential of graphene plasmons.

Acknowledgments

Financial support from the Knut and Alice Wallenberg foundation (KAW), the Swedish Research Council (VR), and the Swedish Foundation for Strategic Support (SSF) is gratefully acknowledged. We wish to thank Philippe Tassin, Daniel J Persson and Samuel L Avila for interesting discussions. G V and T W have contributed equally to this project.

Appendix A. Derivation of equations (3) and (4) in the main article

This appendix details the derivation of equations (3) and (4) starting from equation (2). Equation (2) defines the plasmon dispersion relation in the non-retarded limit. In the presence of losses, the dispersion relation is obtained by allowing complex wave vectors, $q = q_1 + \mathrm{i}q_2$, hence equation (2) becomes

$$(\varepsilon_1 + \varepsilon_2) + \frac{\mathrm{i}(q_1 + \mathrm{i}q_2)\sigma(q_1 + \mathrm{i}q_2, \omega)}{\varepsilon_0\omega} = 0. \tag{A.1}$$

Under the assumption of low loss, q_2/q_1 is small, and equation (A.1) can be expanded to first order in q_2/q_1 and gives rise to:

$$(\varepsilon_1 + \varepsilon_2) + \frac{\mathrm{i}}{\varepsilon_0\omega}(q_1 + \mathrm{i}q_2) \times [\sigma_1(q_1, \omega) + \mathrm{i}\sigma_2(q_1, \omega) + \mathrm{i}q_2\partial_{q_1}(\sigma_1(q_1, \omega) + \mathrm{i}\sigma_2(q_1, \omega))] = 0. \tag{A.2}$$

The real part and zeroth order in q_2/q_1 of equation (A.2) is exactly equation (3), while the imaginary part and first order in q_2/q_1 of equation (A.2) gives equation (4).

Appendix B. Fano-Anderson model in graphene

This appendix gives details on the microscopic model used in the main text. In particular the full Green's function in equation (7*a*) is derived.

We first consider pristine graphene, described in [45, 46, 48], coupled to adatoms by tunneling. The adatoms are modeled here as Fano-Anderson localized states [30] as described in the main text. To solve the system in the case of many adatoms, the following approximations are used: (i) all the impurities are identical, i.e., all of them are characterized by the same parameters ϵ_0, δ and $\tilde{t}$, (ii) the adatoms are uncorrelated and far apart so an average on position can describe the system. These assumptions are also used in the T-matrix formalism for weakly interacting electron systems in the presence of low densities of impurities [30].

In the main text the Hamiltonian of graphene and a single adatom is presented in equation (6). The Hamiltonian for many adatoms is [45, 48]

$$\hat{H} = \sum_l \epsilon_0 \hat{d}_l^\dagger \hat{d}_l + \sum_{\mathbf{p},\lambda} \left(\lambda E_{\mathbf{p}} \hat{c}_{\mathbf{p}\lambda}^\dagger \hat{c}_{\mathbf{p}\lambda} + \sum_l t_{l,\mathbf{p},\lambda} d_l^\dagger \hat{c}_{\mathbf{p},\lambda} + \text{h.c.} \right), \tag{B.1}$$

where $\mathbf{p}$ is the momentum, $t_{l,\mathbf{p},\lambda} = \lambda \tilde{t} e^{i\mathbf{p}\cdot x_l}$, $\lambda = \pm$ is the graphene band index and x_l is the position of the lth impurity. Hence, for many impurities with vanishing hopping between them, the total Hamiltonian is obtained by adding single impurity contributions which is performed by the sum on l.

We introduce the notation $P = (\mathbf{p}, \lambda)$ and $E_P = \lambda E_{\mathbf{p}}$. $\hat{H}$ is quadratic so it can be diagonalized by a unitary transformation $\hat{c}_P = \sum_J A_{P,J} \hat{\alpha}_J$ and $\hat{d}_l = \sum_J B_{l,J} \hat{\alpha}_J$ with A and B matrices such that $H = \sum_J \tilde{E}_J \hat{\alpha}_J^\dagger \hat{\alpha}_J$ and $\{\hat{\alpha}_J, \hat{\alpha}_{J'}^\dagger\} = \delta_{J,J'}$. To find the matrices A and B one can compute commutators using the expression in equation (B.1) obtaining

$$[\hat{d}_l, \hat{H}] = \epsilon_0 \hat{d}_l + \sum_P t_{l,P} \hat{c}_P = \epsilon_0 \sum_J B_{l,J} \hat{\alpha}_J + \sum_P t_{l,P} \sum_J A_{P,J} \hat{\alpha}_J, \tag{B.2}$$

$$[c_P, \hat{H}] = E_P \hat{c}_P + \sum_P t_{l,P}^* \hat{d}_l = E_P \sum_J A_{P,J} \hat{\alpha}_J + \sum_l t_{l,P}^* \sum_J B_{l,J} \hat{\alpha}_J, \tag{B.3}$$

where the second equality in both equations is obtained by substituting the expressions for $\hat{c}_P$ and $\hat{d}_l$ above. The same commutators computed using the diagonal expression of the Hamiltonian gives

$$[\hat{d}_l, \hat{H}] = \sum_I \tilde{E}_I \hat{\alpha}_I B_{l,I},$$
$$[\hat{c}_P, \hat{H}] = \sum_I \tilde{E}_I \hat{\alpha}_I A_{P,I}$$

and by matching with the previous expressions we obtain equations for $A_{P,J}$ and $B_{l,J}$. However, these equations still contain the operator $\hat{\alpha}_J$. This can be removed by performing additional commutations with $\hat{\alpha}_{J'}^\dagger$ giving

$$[\hat{\alpha}_{J'}^\dagger [\hat{d}_l, \hat{H}]] \Rightarrow \epsilon_0 B_{l,J'} + \sum_P t_{l,P} A_{P,J'} = \tilde{E}_{J'} B_{l,J'},$$
$$[\hat{\alpha}_{J'}^\dagger [\hat{c}_P, \hat{H}]] \Rightarrow E_P A_{P,J'} + \sum_l t_{l,P}^* B_{l,J'} = \tilde{E}_{J'} A_{P,J'}$$

from which

$$(\tilde{E}_J - \epsilon_0) B_{l,J} = \sum_P t_{l,P} A_{P,J}, \tag{B.4}$$

$$(\tilde{E}_J - E_P) A_{P,J} = \sum_l t_{l,P}^* B_{l,J}. \tag{B.5}$$

A formal solution to these equations is

$$B_{l,J} = \frac{\sum_P \bar{\delta}_{\tilde{E}_J,\epsilon_0} t_{l,P} A_{P,J}}{\tilde{E}_J - \epsilon_0} + \sum_P Z_{l,J}^B t_{l,P} \delta_{\tilde{E}_J,\epsilon_0},$$
$$A_{P,J} = \frac{\sum_l t_{l,P}^* B_{l,J} \bar{\delta}_{\tilde{E}_J,E_P}}{\tilde{E}_J - E_P} + \sum_l Z_{P,J}^A t_{l,P} \delta_{\tilde{E}_J,E_P},$$

where $Z^{A/B}$ are unknown coefficients and $\bar{\delta}_{a,b} = 1 - \delta_{a,b}$. Now, substitute these solutions into equations (B.4) and (B.5) we obtain

$$(\tilde{E}_J - \epsilon_0) B_{l,J} = \sum_P t_{l,P} \sum_{l'} \left(\frac{t_{l',P}^* B_{l',J} \bar{\delta}_{\tilde{E}_J,E_P}}{\tilde{E}_J - E_P} + Z_{JP}^A t_{l',P} \delta_{\tilde{E}_J,E_P} \right), \tag{B.6}$$

$$(\tilde{E}_J - E_P) A_{P,J} = \sum_l t_{l,P}^* \sum_{P'} \left(\frac{t_{l,P'} A_{P',J} \bar{\delta}_{\tilde{E}_J,\epsilon_0}}{\tilde{E}_J - \epsilon_0} + Z_{P'l}^B t_{l,P'} A_{P',J} \delta_{\tilde{E}_J,\epsilon_0} \right). \tag{B.7}$$

To proceed further we take advantage of the assumption of identical impurities and we may thus perform the sums on l. We assume that the positions of the impurities are independent and randomly distributed, so the average on the impurity position is $\overline{t_{l,P}^* t_{l',P'}} = \frac{1}{N_{\text{site}}} |\tilde{t}|^2 \delta_{P,P'} \delta_{l,l'}$, so $\sum_l \overline{t_{l,P}^* t_{l,P'}} = \frac{N_{\text{imp}}}{N_{\text{site}}} |\tilde{t}|^2 \delta_{P,P'} = n_{\text{imp}} |\tilde{t}|^2 \delta_{P,P'} \equiv t^2 \delta_{P,P'}$. N_{imp} is the number of impurities while n_{imp} is the number of impurities per lattice site. This is standard procedure in T-matrix formalism for low density impurities [30]. Applying this average to perform the sums on l in equations (B.6) and (B.7) gives

$$(\tilde{E}_J - \epsilon_0) B_{l,J} = \sum_P \frac{n_{\text{imp}} |t|^2 B_{l,J} \bar{\delta}_{\tilde{E}_J,E_P}}{\tilde{E}_J - E_P} + Z_{Jl}^B |t|^2 \delta_{\tilde{E}_J,E_P}, \tag{B.8}$$

$$(\tilde{E}_J - E_P)A_{P,J} = \frac{|t|^2 A_{P,J}\bar{\delta}_{\tilde{E}_J,\epsilon_0}}{\tilde{E}_J - \epsilon_0} + Z^A_{Pl}|t|^2\delta_{\tilde{E}_J,\epsilon_0}. \tag{B.9}$$

From equation (B.9) we get $\tilde{E}_J = E_P + \frac{|t|^2\,\bar{\delta}_{\tilde{E}_J,\epsilon_0}}{\tilde{E}_J - \epsilon_0} + Z^A_{Pl}|t|^2\delta_{\tilde{E}_J,\epsilon_0}$ and hence the self energy for the graphene states is obtained: $\Sigma^R_{\rm imp}(\tilde{E}_J) = \frac{|t|^2\,\bar{\delta}_{\tilde{E}_J,\epsilon_0}}{\tilde{E}_J - \epsilon_0} + Z^A_{Pl}|t|^2\delta_{\tilde{E}_J,\epsilon_0}$. Due to level repulsion the new eigenenergies are different from the bare adatom energy so $\delta_{\tilde{E}_J,\epsilon_0} = 0$ and Z^A_{Pl} drops out of the equation.

The matrices A and B, can be found by imposing the conditions $[\hat{d}_l,\ \hat{d}^\dagger_{l'}] = \delta_{l,l'} = \sum_J B_{l,J}B^\dagger_{l',J}$ and $[\hat{c}_P,\ \hat{c}^\dagger_{P'}] = \delta_{P,P'} = \sum_J A_{P,J}A^\dagger_{P',J}$ and $[\hat{c}_P,\ \hat{d}^\dagger_{l'}] = 0 = \sum_J B_{l,J}A^\dagger_{P',J}$ For our purposes, it is not necessary to find the values of A, B and Z. The existence of the unitary matrices A and B is enough to write down the Green's function. Indeed, we know that the Green's function in the frequency domain is $G^R_\alpha(\omega) = \delta_{J,J'}/(\omega + i\eta^+ - \tilde{E}_J)$ since the Hamiltonian is diagonal in $\hat{\alpha}^\dagger,\ \hat{\alpha}$. Hence

$$G^R_{\hat{c}_P}(\omega) = \sum_{J,J'} A_{P,J}A^\dagger_{P',J'}\langle \mathcal{T}\hat{\alpha}_J(t)\hat{\alpha}_{J'}(0)\rangle = \sum_{J,J'} A_{P,J}A^\dagger_{P',J'}\frac{\delta_{J,J'}}{(\omega + i\eta^+ - \tilde{E}_J)}$$
$$= \frac{\delta_{P,P'}}{(\omega + i\eta^+ - \tilde{E}_J)} = \frac{\delta_{P,P'}}{(\omega + i\eta^+ - E_P - \Sigma^R_{\rm imp}(\tilde{E}_J))}$$

and from here equations (7*a*) follow.

Below we give further details on our model. The density of states $\rho(\epsilon) \equiv -\frac{1}{\pi}\,{\rm Tr}\,{\rm Im}\langle G^R_0(\mathbf{p},\ \epsilon)\rangle_{\mathbf{p}}$, Tr is the trace on the sublattice indexes and $\langle\cdot\rangle_{\mathbf{p}}$ is the momentum averaged Greens function defined as

$$\langle G^R_0(\mathbf{p},\ \epsilon)\rangle_{\mathbf{p}} = A_c\int {\rm d}\mathbf{p}\, G^R_0(\mathbf{p},\ \epsilon) = 1\frac{z}{2E_C^2}\ln\left[\frac{-(z)^2}{E_c^2 - (z)^2}\right],$$

where 1 is the unit matrix, $z = \epsilon - \Sigma^R_{\rm imp}(\epsilon)$, A_c is the area of the unit cell in the lattice, ${\rm d}\mathbf{p} = \frac{{\rm d}p_x\,{\rm d}p_y}{(2\pi)^2}$ and E_c is the cut-off energy corresponding to the graphene bandwidth.

Even though the present model treats the electron hopping non-perturbatively, the Coulomb interaction between the adatom and graphene charge is up to now omitted. A full treatment of this interaction is beyond the aim of this work. Nevertheless, we consider the Coulomb interaction in the presence of charge fluctuations induced by the tunneling. This effect introduces a further relaxation channel, i.e., a finite lifetime to both the adatom states, δ^{-1}, and the electron states in the graphene $\Gamma_{\rm e}^{-1}$. Following a method similar to [56], we evaluate them to be $\Gamma_{\rm e} \simeq 10^{-4}E_F$, $\delta \simeq 10^{-3}E_F$ at $T = 0$. Furthermore, we include a finite relaxation time for the graphene electrons which is caused by imperfections and phonons in the graphene lattice. From good quality graphene this number can be inferred to be approximately 1 ps, see [54]. For realistic doping levels of graphene, this relaxation time completely dominates $\Gamma_{\rm e}^{-1}$ which is neglected. These values are used throughout the paper and the total relaxation time is included following the Mermin prescription [5, 29].

Appendix C. Derivation of equation (8) and simplified expression for the conductivity

In this appendix we give some details on the derivation of equation (8) and we report a simplified expression for the one-spin, one-valley susceptibility. Before proceeding, an observation needs to be pointed out. In the context of plasmons, it is common to describe the purely longitudinal electric field, along the x axes, with a potential $\phi(\mathbf{x},\ t) = \phi_{\mathbf{q}}\,{\rm e}^{i\mathbf{q}\cdot\mathbf{x} - i\omega t}$ $\mathbf{q} = q\hat{x}$ and $\boldsymbol{A} = 0$ with $\boldsymbol{E}_{\mathbf{q}} = i\mathbf{q}\phi_{\mathbf{q}}$ [30, 49–51]. The linear response of the system is then encoded in the density–density response function (polarisability $\chi_{\rho\rho}$) that expresses the density fluctuation induced by the potential as $\langle\hat{\rho}(\mathbf{q},\ \omega)\rangle = \chi_{\rho\rho}(\mathbf{q},\ \omega)\phi_{q_x}$. In the standard situation, the continuity equation relates $\chi_{\rho\rho}$ to the conductivity. However, in the presence of the adatoms, the total charge density includes both the charge density in the graphene and on the impurity states $\hat{\rho}_{\rm tot}(\mathbf{q}) = \hat{\rho}(\mathbf{q}) + \hat{\rho}_{\rm imp}$, with $\hat{\rho}_{\rm imp} = e\hat{d}^\dagger\hat{d}$. Also the last term, $\rho_{\rm imp}$, needs to be included to fulfill the continuity equation $i\partial_t\hat{\rho}_{\rm tot}(\mathbf{q}) = -i\mathbf{q}\cdot\hat{\mathbf{j}}(\mathbf{q})$ which makes this approach more involved. Therefore, it is more convenient to evaluate the longitudinal current–current response function, $\chi_{j_xj_x}(\mathbf{q},\ \omega)$, in the temporal gauge since the adatoms carry no in-plane current so it is possible to avoid including terms related to the adatoms.

Here we compute the average value of the longitudinal current $\hat{j}_x(\mathbf{q},\ \omega) = ev_F\sum_{\mathbf{p}}\hat{\psi}^\dagger_{\mathbf{p}-\mathbf{q}}\sigma_x\hat{\psi}_{\mathbf{p}}$, where σ_x is the first Pauli matrix, in presence of the perturbation $\delta H_x = ev_F A_q\hat{j}_x(\mathbf{q})\,{\rm e}^{iqx - i\omega t}$. For $\boldsymbol{E} = 0$ and in equilibrium, the values of currents and density deviation are vanishing. In Keldysh formalism, the current to linear order in the perturbation is written $\langle\hat{j}_x(\mathbf{q},\ \omega)\rangle = -\frac{i}{2}{\rm Tr}\,[\sigma_x\delta G^K(\mathbf{q},\ \omega)]$. As shown in [57]

$$\delta\check{G}(\mathbf{q},\omega) = (\check{G}_0 \circ \delta\check{H}_x \circ \check{G}_0)(\mathbf{q},\omega)$$
$$= \int \frac{\mathrm{d}\mathbf{p}\mathrm{d}\epsilon}{2\pi}\check{G}_0(\mathbf{p},\epsilon)\cdot\tau_x\delta H_x\cdot\check{G}_0(\mathbf{p}-\mathbf{q},\epsilon-\omega) \tag{C.1}$$

($\tau_x = \sigma_x$ in Keldysh space). $\check{G}_0$ is the unperturbed Green's in Keldysh space and $\circ$stands for the sum on all internal degrees of freedom. The substitution of $\delta\check{G}(\mathbf{q},\omega)$ in $\langle\hat{j}_x(\mathbf{q},\omega)\rangle$ gives

$$\chi_{j_xj_x}(\mathbf{q},\omega) = \frac{\mathrm{i}e^2\nu_F^2}{2}\int\frac{\mathrm{d}\mathbf{p}\mathrm{d}\epsilon}{(2\pi)}\,\mathrm{Tr}\,[\sigma_x G_0^R(\mathbf{p},\epsilon)\sigma_x G_0^K(\mathbf{p}-\mathbf{q},\epsilon-\omega) \tag{C.2}$$
$$+\,\sigma_x G_0^K(\mathbf{p},\epsilon)\sigma_x G_0^A(\mathbf{p}-\mathbf{q},\epsilon-\omega)] \tag{C.3}$$

which is identical to equation (8). The Keldysh component of the Green's function at equilibrium is $G^K(\mathbf{p},\epsilon) = f(\epsilon)(G^R(\mathbf{p},\epsilon) - G^A(\mathbf{p},\epsilon))$ with $f(\epsilon) = 1/(1+\mathrm{e}^{\beta(\epsilon-\mu)})$, $(g_0^R(\mathbf{p},\epsilon))^* = g_0^A(\mathbf{p},\epsilon)$, and $(G^A(\mathbf{q},\epsilon))^* = G^R(\mathbf{q},\epsilon)$. Substituting these relations and performing the trace in equation (C.2), the integrand becomes

$$\begin{aligned}&\mathrm{Tr}\,[f(\epsilon-\omega)\sigma_x G_0^R(\mathbf{p},\epsilon)\sigma_x(G_0^R(\mathbf{p}-\mathbf{q},\epsilon-\omega) - G_0^A(\mathbf{p}-\mathbf{q},\epsilon-\omega))\\ &\quad + f(\epsilon)\sigma_x(G_0^R(\mathbf{p},\epsilon) - G_0^A(\mathbf{p},\epsilon))\sigma_x G_0^A(\mathbf{p}-\mathbf{q},\epsilon-\omega)]\\ &= [f(\epsilon-\omega)g_0^R(\mathbf{p},\epsilon)(g_0^R(\mathbf{p}-\mathbf{q},\epsilon-\omega) - g_0^A(\mathbf{p}-\mathbf{q},\epsilon-\omega))\\ &\quad + f(\epsilon)(g_0^R(\mathbf{p},\epsilon) - g_0^A(\mathbf{p},\epsilon))g_0^A(\mathbf{p}-\mathbf{q},\epsilon-\omega)]F_{xx}^{\lambda,\lambda'}(\mathbf{q},\mathbf{p}),\end{aligned} \tag{C.4}$$

where

$$F_{xx}^{\lambda,\lambda'}(\mathbf{q},\mathbf{p}) = 1 + \frac{\lambda\lambda'(p\cos 2\theta - q\cos\theta)}{|\mathbf{p}-\mathbf{q}|} \tag{C.5}$$

is the square of the matrix element of the longitudinal current operator.

To simplify $\chi_{j_xj_x}(\mathbf{q},\omega)$ one may proceed to first perform the integral on ϵ. Note that in the clean case this integral can be performed following [30] to arrive at the corresponding expression used in [50, 51, 53]. The present case is more involved due to the finite self-energy but the integrand in equation (C.2) has known poles. The poles may come from the Green's function, i.e., from $g_0^{R/A}(\mathbf{p},\epsilon)$, or from the Fermi distribution $f(\epsilon)$, they are denoted $\epsilon_\lambda^{\pm,R/A}(\mathbf{p})$ and $\epsilon_m = \mathrm{i}k_BT\pi(2m+1)+\mu$ (m integer), respectively. The ϵ integral on the real axes in (C.2) can be closed in the complex plane in such a way that as few Green's function poles as possible are included inside the path. Splitting the integral in two parts, the path of the term proportional to $f(\epsilon-\omega)$ (first term in equation (C.4)) is closed in the upper half plane, to avoid the poles of g_0^Rs. Vice versa the integral of the term proportional to $f(\epsilon)$ in equation (C.4), is closed in the lower half plane, to avoid the poles of g_0^As. Of course, all the poles of the Fermi distributions can not be avoided since they lie on both sides of the real axis. The energy integration therefore has two contributions $\chi_{j_xj_x}(\mathbf{q},\omega) = \chi^{\mathrm{P}}_{j_xj_x}(\mathbf{q},\omega) + \chi^{\mathrm{T}}_{j_xj_x}(\mathbf{q},\omega)$ with

$$\chi^{\mathrm{P}}_{j_xj_x}(\mathbf{q},\omega) = \sum_{\lambda\lambda',l}\frac{e^2\nu_F^2}{2}\int\mathrm{d}\mathbf{p}[f(\epsilon_{\lambda'}^{l,A}(\mathbf{p}-\mathbf{q}))Z_{\lambda'}^{l*}(\mathbf{p}-\mathbf{q})g_{0\lambda}^R(\epsilon_{\lambda'}^{l,A}(\mathbf{p}-\mathbf{q})+\omega,\mathbf{p})$$
$$+ f(\epsilon_\lambda^{l,R}(\mathbf{p}))Z_\lambda^l(\mathbf{p})g_{0\lambda'}^A(\epsilon_\lambda^{l,R}(\mathbf{p})-\omega,\mathbf{p}-\mathbf{q})]F_{xx}^{\lambda,\lambda'}(\mathbf{q},\mathbf{p}), \tag{C.6}$$

$$\chi^{\mathrm{T}}_{j_xj_x}(\mathbf{q},\omega) = k_BTe^2\nu_F^2\sum_{\lambda\lambda'}\sum_{n=1}^{\infty}\int\mathrm{d}\mathbf{p}[g_{0\lambda}^R(\epsilon_{2n+1}+\omega,\mathbf{p})(g_{0\lambda}^R - g_{0\lambda}^A)(\epsilon_{2n+1},\mathbf{p}-\mathbf{q})$$
$$-(g_{0\lambda}^R - g_{0\lambda}^A)(\epsilon_{-2n-1},\mathbf{p}-\mathbf{q})g_{0\lambda}^A(\epsilon_{-2n-1}-\omega,\mathbf{p}-\mathbf{q})]F_{xx}^{\lambda,\lambda'}(\mathbf{q},\mathbf{p}). \tag{C.7}$$

Here χ^{P} and χ^{T} are given by the poles of the Green's function and Fermi function respectively. We underline that to separate $\chi_{j_xj_x}(\mathbf{q},\omega)$ in these two terms, the only assumption is that the self-energy is a smooth function of ϵ. Hence, it can be extended to include also other contributions to the electronic self-energy such as the phonon and electron–electron interaction. We underline that the susceptibility contributions in equations (C.6) and (C.7) are for one valley and one spin and thus needs to be multiplied by g_sg_v, as is done in the main text, to obtain the total result for graphene.

The momentum integrals in $\chi^{\mathrm{P}}_{j_xj_x}$ and $\chi^{\mathrm{T}}_{j_xj_x}$ are performed numerically using standard integration routines. It turns out that $|\chi^{\mathrm{T}}_{j_xj_x}|$ is less than 1% of $|\chi^{\mathrm{P}}_{j_xj_x}|$ for the parameter range of interest. In particular, for $\omega < \epsilon_F$, $|\chi^{\mathrm{T}}_{j_xj_x}| < 10^{-3}|\chi^{\mathrm{P}}_{j_xj_x}|$ and is therefore omitted in the analysis in the main text.

References

[1] Ju L *et al* 2011 Graphene plasmonics for tunable terahertz metamaterials *Nat. Nanotechnol.* **6** 630–4
[2] Yan H, Li X, Chandra B, Tulevski G, Wu Y, Freitag M, Zhu W, Avouris P and Xia F 2012 Tunable infrared plasmonic devices using graphene/insulator stacks *Nat. Nanotechnol.* **7** 330–4
[3] Low T and Avouris P 2014 Graphene plasmonics for terahertz to mid-infrared applications *ACS Nano* **8** 1086–101

[4] Li Z Q, Henriksen E A, Jiang Z, Hao Z, Martin M C, Kim P, Stormer H L and Basov D N 2008 Dirac charge dynamics in graphene by infrared spectroscopy *Nat. Phys.* **4** 532
[5] Jablan M, Buljan H and Soljačić M 2009 Plasmonics in graphene at infrared frequencies *Phys. Rev.* B **80** 245435
[6] Goncalves P A D and Peres N M R 2016 *An Introduction to Graphene Plasmonics* (Singapore: World Scientific)
[7] Koppens F H L, Chang D E and García de Abajo F J 2011 Graphene plasmonics: a platform for strong light–matter interactions *Nano Lett.* **11** 3370–7
[8] García de Abajo F J 2014 Graphene plasmonics: challenges and opportunities *ACS Photon.* **1** 135–52
[9] Chen J *et al* 2012 Optical nano-imaging of gate-tunable graphene plasmons *Nature* **487** 77–81
[10] Fei Z *et al* 2012 Gate-tuning of graphene plasmons revealed by infrared nano-imaging *Nature* **487** 82–5
[11] Wenger T, Viola G, Fogelström M, Tassin P and Kinaret J 2016 Optical signatures of nonlocal plasmons in graphene *Phys. Rev.* B **94** 205419
[12] Zhu X, Yan W, Jepsen P U, Hansen O, Mortensen N A and Xiao S 2013 Experimental observation of plasmons in a graphene monolayer resting on a two-dimensional subwavelength silicon grating *Appl. Phys. Lett.* **102** 131101
[13] Zhan T R, Zhao F Y, Hu X H, Liu X H and Zi J 2012 Band structure of plasmons and optical absorption enhancement in graphene on subwavelength dielectric gratings at infrared frequencies *Phys. Rev.* B **86** 165416
[14] Yu R, Pruneri V and García de Abajo F J 2016 Active modulation of visible light with graphene-loaded ultrathin metal plasmonic antennas *Sci. Rep.* **6** 32144
[15] Alonso-González P *et al* 2014 Controlling graphene plasmons with resonant metal antennas and spatial conductivity patterns *Science* **344** 1369–73
[16] Goncalves P A D, Dias E J C, Bludov Yu V and Peres N M R 2016 Modeling the excitation of graphene plasmons in periodic grids of graphene ribbons: an analytical approach *Phys. Rev.* B **94** 195421
[17] Kravets V G *et al* 2013 Singular phase nano-optics in plasmonic metamaterials for label-free single-molecule detection *Nat. Mater.* **12** 304–9
[18] Rodrigo D, Limaj O, Janner D, Etezadi D, García de Abajo F J, Pruneri V and Altug H 2015 Mid-infrared plasmonic biosensing with graphene *Science* **349** 165–8
[19] Grigorenko A N, Polini M and Novoselov K S 2012 Graphene plasmonics *Nat. Photon.* **6** 749–58
[20] Koppens F H L, Mueller T, Avouris P, Ferrari A C, Vitiello M S and Polini M 2014 Photodetectors based on graphene, other two-dimensional materials and hybrid systems *Nat. Nanotechnol.* **9** 780–93
[21] Dastmalchi B, Tassin P, Koschny T and Soukoulis C M 2016 A new perspective on plasmonics: confinement and propagation length of surface plasmons for different materials and geometries *Adv. Opt. Mater.* **4** 177–84
[22] Tassin P, Koschny T and Soukoulis C M 2013 Graphene for terahertz applications *Science* **341** 620–1
[23] Peres N M R, Guinea F and Castro Neto A H 2006 Electronic properties of disordered two-dimensional carbon *Phys. Rev.* B **73** 125411
[24] Peres N M R, Stauber T and Castro Neto A H 2008 The infrared conductivity of graphene on top of silicon oxide *Europhys. Lett.* **84** 38002
[25] Grushin A G, Valenzuela B and Vozmediano M A H 2009 Effect of coulomb interactions on the optical properties of doped graphene *Phys. Rev.* B **80** 155417
[26] Schütt M, Ostrovsky P M, Gornyi I V and Mirlin A D 2011 Coulomb interaction in graphene: relaxation rates and transport *Phys. Rev.* B **83** 155441
[27] Principi A, Vignale G, Carrega M and Polini M 2013 Impact of disorder on dirac plasmon losses *Phys. Rev.* B **88** 121405
[28] Principi A, Carrega M, Lundeberg M B, Woessner A, Koppens F H L, Vignale G and Polini M 2014 Plasmon losses due to electron-phonon scattering: the case of graphene encapsulated in hexagonal boron nitride *Phys. Rev.* B **90** 165408
[29] Mermin N D 1970 Lindhard dielectric function in the relaxation-time approximation *Phys. Rev.* B **1** 2362–3
[30] Mahan G 1993 *Many-Particle Physics* 2nd edn (New York: Plenum)
[31] Rana F 2008 Graphene terahertz plasmon oscillators *IEEE Trans. Nanotechnol.* **7** 91–9
[32] Schedin F, Geim A K, Morozov S V, Hill E W, Blake P, Katsnelson M I and Novoselov K S 2007 Detection of individual gas molecules adsorbed on graphene *Nat. Mater.* **6** 652–5
[33] Chen C W, Hung S C, Yang M D, Yeh C W, Wu C H, Chi G C, Ren F and Pearton S J 2011 Oxygen sensors made by monolayer graphene under room temperature *Appl. Phys. Lett.* **99** 243502
[34] Wu L, Chu H S, Koh W S and Li E P 2010 Highly sensitive graphene biosensors based on surface plasmon resonance *Opt. Express* **18** 14395
[35] Wenger T, Viola G, Kinaret J, Fogelstrom M and Tassin P 2017 High-sensitivity plasmonic refractive index sensing using graphene *2D Mater.* **4** 025103
[36] Farmer D B, Avouris P, Li Y, Heinz T F and Han S-J 2016 Ultrasensitive plasmonic detection of molecules with graphene *ACS Photon.* **3** 553–7
[37] Leenaerts O, Partoens B and Peeters F M 2008 Adsorption of H_2O, NH_3, CO, NO_2, and NO on graphene: a first-principles study *Phys. Rev.* B **77** 125416
[38] Wehling T O, Novoselov K S, Morozov S V, Vdovin E E, Katsnelson M I, Geim A K and Lichtenstein A I 2008 Molecular doping of graphene *Nano Lett.* **8** 173–7
[39] Ihnatsenka S and Kirczenow G 2011 Dirac point resonances due to atoms and molecules adsorbed on graphene and transport gaps and conductance quantization in graphene nanoribbons with covalently bonded adsorbates *Phys. Rev.* B **83** 245442
[40] Gmitra M, Kochan D and Fabian J 2013 Spin–orbit coupling in hydrogenated graphene *Phys. Rev. Lett.* **110** 246602
[41] Zollner K, Frank T, Irmer S, Gmitra M, Kochan D and Fabian J 2016 Spin–orbit coupling in methyl functionalized graphene *Phys. Rev.* B **93** 045423
[42] Frank T, Irmer S, Gmitra M, Kochan D and Fabian J 2017 Copper adatoms on graphene: theory of orbital and spin-orbital effects *Phys. Rev.* B **95** 035402
[43] Hu H, Yang X, Zhai F, Hu D, Liu R, Liu K, Sun Z and Dai Q 2016 Far-field nanoscale infrared spectroscopy of vibrational fingerprints of molecules with graphene plasmons *Nat. Commun.* **7** 12334
[44] Dressel M and Grüner G 2002 *Electrodynamics of Solids: Optical Properties of Electrons in Matter* (Cambridge: Cambridge University Press)
[45] Castro Neto A H, Guinea F, Peres N M R, Novoselov K S and Geim A K 2009 The electronic properties of graphene *Rev. Mod. Phys.* **81** 109–62
[46] Sarma S D, Adam S, Hwang E H and Rossi E 2011 Electronic transport in two-dimensional graphene *Rev. Mod. Phys.* **83** 407–70
[47] Löfwander T and Fogelström M 2007 Impurity scattering and mott's formula in graphene *Phys. Rev.* B **76** 193401

[48] Katsnelson M I 2012 *Graphene: Carbon in Two Dimensions* (Cambridge: Cambridge University Press)
[49] Giuliani G F and Vignale G 2005 *Quantum Theory of the Electron Liquid* (Cambridge: Cambridge University Press)
[50] Hwang E H and Sarma S D 2007 Dielectric function, screening, and plasmons in two-dimensional graphene *Phys. Rev.* B **75** 205418
[51] Wunsch B, Stauber T, Sols F and Guinea F 2006 Dynamical polarization of graphene at finite doping *New J. Phys.* **8** 318
[52] Ramezanali M R, Vazifeh M M, Asgari R, Polini M and MacDonald A H 2009 Finite-temperature screening and the specific heat of doped graphene sheets *J. Phys. A: Math. Theor.* **42** 214015
[53] Principi A, Polini M and Vignale G 2009 Linear response of doped graphene sheets to vector potentials *Phys. Rev.* B **80** 075418
[54] Bolotin K I, Sikes K J, Jiang Z, Klima M, Fudenberg G, Hone J, Kim P and Stormer H L 2008 Ultrahigh electron mobility in suspended graphene *Solid State Commun.* **146** 351–5
[55] Cantatore V and Panas I 2016 Possible socket-plug standard connection for functionalized graphene—validation by DFT *Carbon* **104** 40–6
[56] Zhu Z-G and Berakdar J 2011 Magnetic adatoms on graphene in the kondo regime: an anderson model treatment *Phys. Rev.* B **84** 165105
[57] Rammer J 2007 *Quantum Field Theory of Non-equilibrium States* (Cambridge: Cambridge University Press)